Imaging of Fluorine and Boron from Fluorinated Boronophenylalanine in the Same Cell at Organelle Resolution by Correlative Ion Microscopy and Confocal Laser Scanning Microscopy[1]

Subhash Chandra,[2] George W. Kabalka, Daniel R. Lorey II, Duane R. Smith, and Jeffrey A. Coderre

Department of Chemistry and Chemical Biology, Cornell University, Ithaca, New York 14853-1301 [S. C., D. R. L., D. R. S.]; Biomedical Imaging Center, Department of Chemistry, University of Tennessee, Knoxville, Tennessee 37996-1600 [G. W. K.]; and Department of Nuclear Engineering, Massachusetts Institute of Technology, Cambridge, Massachusetts 02139 [J. A. C.]

ABSTRACT

Purpose: **There is a clear need for a technique that provides subcellular locations of fluorine and boron atoms from fluorinated neutron capture agents because positron emission tomography is being tested as a tool for providing tumor boron concentrations in boron neutron capture therapy.**

Experimental Design: **Ion microscopy was used in combination with confocal laser scanning microscopy to investigate the subcellular locations of fluorine and boron from fluorinated *p*-boronophenylalanine (F-BPA) in human glioblastoma T98G cells. The fluorinated compound was also compared with *p*-boronophenylalanine (BPA) for delivery of boron after a clinically relevant 6-h exposure. Mitochondria were identified by rhodamine 123 labeling. A strict cryogenic sample preparation was used, and measurements were made in fractured freeze-dried cells.**

Results: **The nucleus, a perinuclear mitochondria-rich cytoplasmic region, and the remaining cytoplasm were the three subcellular regions identified in individual T98G cells. In cells treated with F-BPA, the mitochondria-rich perinuclear cytoplasmic region exhibited significantly lower fluorine and boron signals than the remaining cytoplasm and the nuclei. Ion microscopy observations revealed a nearly 1:1 distribution of fluorine and boron in subcellular compartments. Quantitative subcellular observations indicated that there was no significant difference in boron delivery to subcellular compartments between the F-BPA and nonfluorinated BPA.**

Conclusions: **These observations provide the first direct evidence that fluorine and boron from fluorinated BPA are cocompartmentalized in cells and that the fluorinated compound is as efficient for boron delivery as the nonfluorinated BPA at a clinically relevant time point. These observations provide strong support for the use of F-BPA in positron emission tomography biodistribution studies for boron neutron capture therapy.**

INTRODUCTION

The drug BPA[3] is one of two boron delivery agents approved for use in clinical trials of BNCT for the treatment of malignant brain tumors (1–4) and melanoma (5). BNCT is a binary radiotherapeutic modality that has the potential to selectively irradiate tumor tissue. A prerequisite is the preferential accumulation of ^{10}B in tumor cells, which are then irradiated with low-energy neutrons. BNCT is based on the fission reaction ($^{10}B + {}^{1}n \rightarrow [^{11}B] \rightarrow {}^{7}Li + {}^{4}He(\alpha) + 2.79$ MeV), where a ^{10}B atom captures a thermal neutron ($E_{th} < 0.4$ eV) and spontaneously decays to produce the linear recoiling particles ^{4}He (α particle) and ^{7}Li. In tissues, these particles have short penetration ranges, approximately the dimension of a single cell ($\sim$5 μm for ^{7}Li and $\sim$9 μm for ^{4}He). For BNCT to be effective, it has been estimated that tumor cells must be loaded with a minimum of 15–30 μg ^{10}B/g tissue to raise the boron neutron capture-related dose to the tumor significantly above the background radiation dose (6, 7) that results from capture reactions with normal tissue ^{1}H and ^{14}N. Because the nuclear localization of ^{10}B has been determined to be most effective for BNCT (6), the knowledge of the subcellular boron distribution is of paramount importance.

In clinical BNCT, the radiation dose contribution from the $^{10}B(n,\alpha)^{7}Li$ reaction must be calculated using blood boron concentrations mainly because there are no techniques available at

Received 12/6/01; revised 4/8/02; accepted 4/18/02.
The costs of publication of this article were defrayed in part by the payment of page charges. This article must therefore be hereby marked *advertisement* in accordance with 18 U.S.C. Section 1734 solely to indicate this fact.
[1] Supported by the Biological and Environmental Research Program, United States Department of Energy, Grants DE-FG02-91ER61138 (to S. C.), DE-FG02-96ER62189 (to G. W. K.), and DE-AC02-98CH10886 (to J. A. C.).
[2] To whom requests for reprints should be addressed, at Department of Chemistry and Chemical Biology, Cornell University, Ithaca, NY 14853-1301. Phone: (607) 255-3884; Fax: (607) 255-4137; E-mail: sc40@cornell.edu.

[3] The abbreviations used are: BPA, *p*-boronophenylalanine; BNCT, boron neutron capture therapy; PET, positron emission tomography; F-BPA, fluorinated analogue of BPA; SIMS, secondary ion mass spectrometry; CLSM, confocal laser scanning microscopy; CCD, charge-coupled device; MRI, magnetic resonance imaging.

present that can measure boron concentrations in tumors at the time a patient undergoes neutron irradiation. However, methodology using PET is currently being developed for this purpose (8, 9). This approach uses ^{18}F, a positron-emitting radionuclide, attached to the chemical structure of a boron delivery agent. PET may provide information about the pharmacokinetics of ^{10}B accumulation in tumor cells for radiation dosimetry. The interpretation of PET observations, however, will be dependent on two important assumptions: (*a*) the fluorine and boron are cocompartmentalized inside the cell; and (*b*) the fluorinated compound delivers boron to the subcellular compartments in concentrations comparable with the nonfluorinated compound. Neither of these assumptions can be tested directly by PET alone because the technique is specific for the analysis of the ^{18}F tracer but not ^{10}B, and, with its 6–10 mm spatial resolution, PET is inadequate for subcellular measurements. However, a technique for the subcellular analysis of both fluorine and boron can address these critical questions and serve as a complimentary tool for studies of PET compounds.

The SIMS-based imaging technique of ion microscopy is ideally suited for subcellular microlocalization studies in biology and medicine (10–12). The multielemental (isotopic) imaging capability of ion microscopy provides a novel approach for imaging both fluorine and boron from the same cell after treatment with a fluorinated PET compound. By using ^{19}F-labeled BPA in the present study, observations from ion microscopy and CLSM were correlated from the same cell to image the distributions of both fluorine and boron at organelle resolution. These observations, for the first time, provide new insights about the intracellular cocompartmentalization of fluorine and boron from F-BPA as well as a quantitative comparison of the intracellular boron delivery characteristics of F-BPA and the clinical drug BPA at pharmacological concentrations. The novel methodology presented here can be extended to subcellular localization studies of any desired fluorinated or double-labeled therapeutic agent.

MATERIALS AND METHODS

Materials. T98G human malignant glioma (glioblastoma) cells were obtained from the American Type Culture Collection (Manassas, VA). ^{10}BPA (>95 atom% ^{10}B) was purchased from Boron Biologicals, Inc. (Raleigh, NC). The F-BPA (2-[^{19}F]fluoro-4-boronophenylalanine) was synthesized with the ^{19}F stable isotope label and naturally abundant boron [80 atom% ^{11}B, 20 atom% ^{10}B (13)]. The chemical structures of BPA and F-BPA are shown in Fig. 1. Both drugs were used in soluble form as the fructose complex, the preparation of which is detailed elsewhere (14). Rhodamine 123 was purchased from Sigma (St. Louis, MO). Latex beads (11 μm in diameter) were purchased from Duke Scientific (Palo Alto, CA). Polished high purity N-type semiconductor-grade silicon wafers were purchased from Silicon Quest International (Santa Clara, CA).

Cell Growth and Drug Treatments. T98G cells were grown on the polished surface of high purity N-type silicon pieces. An electrically conducting cell growth substrate is required for ion microscopy imaging because the sample is held at ±4,500 V in the sample chamber of the ion microscope. The silicon substrate is nontoxic to cells and has been used for SIMS

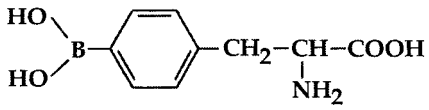

(a) *p*-boronophenylalanine

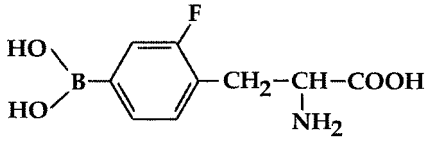

(b) Fluorinated *p*-boronophenylalanine

Fig. 1 Chemical structures of BPA and F-BPA.

studies of ion transport and drug localization (15–19). The silicon pieces (random shapes of about 1 cm^2 surface area) were sterilized before cell seeding. Each 60-mm plastic Petri dish used for cell growth contained six silicon substrates. The cells were seeded at a density of 250,000 cells/dish. Approximately 30,000 latex beads (11 μm in diameter) were added to each Petri dish on the third day after cell seeding. These beads act as spacers in the cryogenic sandwich-fracture method (20). After the cells reached about 80% confluence on the silicon substrate, sister cells growing on different silicon substrates under identical conditions were divided and subjected to nutrient medium containing 110 μg/ml boron equivalent concentrations of either ^{10}BPA or ^{19}F-BPA for 6 h. The boron concentration in stock solutions of each drug was assessed by prompt γ-ray spectroscopy analysis (21). In two additional treatments, mitochondria were stained by the exposure of cells to 20 μg/ml rhodamine 123 (22) for 30 min before the completion of the 6-h drug treatment for both compounds.

Cryogenic Sample Preparation. After the respective treatments, the silicon pieces containing the cells were sandwiched with a clean silicon piece, flash frozen in liquid isopentane held at −150°C, and quickly transferred into liquid nitrogen. The two silicon surfaces of the silicon-cell-silicon sandwich were separated under liquid nitrogen by prying them apart with a razor blade as described previously (20). The substrate side of the sandwich contained groups of cells fractured at the plasma membrane. The apical half-membrane and the overlaying growth medium were removed to the nonsubstrate side of the sandwich. The apical-fractured cells thus produced are essentially the whole cells without the ectoplasmic face leaflet of the plasma membrane (20, 23). The cells were then freeze-dried at −90°C overnight in a Tis-U-Dry freeze-drier (FTS Systems, Inc., Stone Ridge, NY). The temperature of the sample stage of the freeze-drier was gradually increased to 40°C to avoid any rehydration. The freeze-drier was vented to dry nitrogen, and the samples were quickly transferred to a desiccator. The samples were stored until optical microscopy, CLSM, and SIMS measurements were made.

Optical and CLSM Measurements. The silicon substrates containing freeze-dried cells were transferred to an airtight chamber to avoid any rehydration during optical and

CLSM measurements (24). An Olympus microscope with reflected light optics was used for photographing the fractured freeze-dried cells. For mitochondrial imaging in individual fractured freeze-dried cells, a Bio-Rad MRC 600/Zeiss Axiovert 10 confocal microscope was used. As reported previously, the frozen freeze-dried cell matrix does not interfere in CLSM fluorescence measurements of Golgi apparatus and mitochondria (12). The imaging protocol used in the present study included a correlative analysis of the same cell with optical, CLSM, and ion microscopy.

Isotopic Imaging with Dynamic SIMS Ion Microscopy. A dynamic SIMS CAMECA IMS-3f ion microscope (Paris, France) that provides a nominal spatial resolution of 0.5 μm was used for subcellular isotopic imaging studies (10). A 5.5 keV mass filtered primary ion beam of O_2^+ (about 50 nA beam current with a spot size of about 75 μm) was raster scanned over a 250 × 250-μm square region of the sample. A 60-μm contrast aperture was used in the imaging mode. Before SIMS imaging, cells were coated with a thin layer of Au/Pd alloy to enhance their electrical conductivity. In the positive secondary ion detection mode, images of isotopes with masses 10, 11, 12, 23, 39, and 40 revealed the subcellular distribution of ^{10}B, ^{11}B, ^{12}C, ^{23}Na, ^{39}K, and ^{40}Ca, respectively. In fractured freeze-dried cells, SIMS matrix effects such as differential sputtering were not significant, and the secondary ion signals studied here did not reveal any significant mass interferences (25, 26). In studies where imaging of fluorine was also required along with boron from the same cell, the imaging of positive secondaries was completed first, and then instrumental conditions were optimized for detecting negative secondaries for imaging fluorine at mass 19 from the same cells. High mass resolution analyses ($m/\Delta m \cong 4000$) were performed on ^{19}F-BPA-treated cells to confirm the purity of fluorine signals at mass 19 as the $^{19}F^-$ species. These observations revealed a single peak indicating the purity of fluorine signals to be >99.9% with no significant interference from polyatomic or hydrocarbon species. In cells not treated with the fluorinated drug, barely detectable fluorine signals were observed throughout the cell. The origin of these signals is plausibly naturally occurring trace amounts of fluorine in cells. These dim intensity signals did not contribute significantly because their intensity levels were >3 orders of magnitude lower than fluorine signals observed from cells treated with ^{19}F-BPA.

SIMS Image Processing. Isotope images were digitized directly from the microchannel plate/phosphor screen assembly of the ion microscope using a slow scan CCD camera (Photometrics; Tucson, AZ; model CH220 CCD liquid-cooled camera head equipped with a Thomson-CSF TH7882 CDA CCD) and digitized to 14 bits/pixel with a Photometrics camera controller. Isotope image integration times varied according to their intensities. In general, ^{39}K and ^{23}Na images were recorded for 0.4 s. The ^{10}B, ^{11}B, ^{12}C, and ^{40}Ca images were recorded for 2 min. Fluorine images were recorded for 10–30 s. Within a single field of isotopic imaging, the variations in time of exposures for various isotope images were compensated for quantification in relation to the time of exposure of the ^{12}C image. Computer image processing was performed using DIP Station (Hayden Image Processing Group) on a Macintosh Quadra 840AV. Isotope images of the positive secondary ions ^{10}B, ^{11}B, ^{23}Na, and ^{39}K were quantified using relative sensitivity factors to the cell matrix ^{12}C signals in the same spatial registration (27). The absolute dry weight concentrations obtained by this method were converted into wet weight concentrations by assuming 85% cell water content distributed throughout the cell. Whereas boron concentrations were calculated in desired subcellular compartments, intracellular potassium and sodium concentrations from the same cells were calculated on a cellular level. The statistical significance of comparable treatments was compared using the ANOVA.

For checking the cocompartmentalization of fluorine and boron in subcellular compartments, an approach based on fluorine:carbon and boron:carbon secondary ion signal ratios was used. These ratios were determined for the nucleus, the mitochondria-rich perinuclear region, and the remaining cytoplasm in individual cells. These ratios were then used to evaluate the partitioning of boron and fluorine in the mitochondria-rich perinuclear cytoplasm and the remaining cytoplasm as compared with the cell nucleus within a cell. This approach provides an effective way for a direct comparison of the cocompartmentalization of fluorine and boron in subcellular compartments and eliminates the need for a SIMS relative sensitivity factors of fluorine to carbon.

RESULTS

SIMS Imaging of Fluorine and Boron in the Same Cell from ^{19}F-BPA-treated Cells. Fig. 2 shows SIMS chemical imaging analysis of T98G cells treated with ^{19}F-BPA for 6 h. Fig. 2*a* shows an optical photograph of two fractured freeze-dried cells with discernible features. T98G cells are frequently multinucleated with irregular-shaped nuclei occupying a significant volume in the cell. The boundaries of the nuclei have been outlined with a *dotted line*, and the *arrows* indicate the organelle-rich perinuclear cytoplasmic region in each cell (Fig. 2*a*). SIMS analysis of the same two cells revealing ^{39}K, ^{23}Na, ^{40}Ca, ^{11}B, and ^{19}F isotopic distributions is shown in Fig. 2, *b–f*, respectively. Within an individual SIMS image, the level of brightness is directly proportional to the isotopic concentration. The ^{39}K distribution (Fig. 2*b*) shows potassium to be distributed throughout the cell with minor heterogeneity. The ^{23}Na image of the same cells (Fig. 2*c*) recorded for the same amount of time as the ^{39}K image reveals dim intensities. This is expected because cellular potassium is about an order of magnitude higher than sodium in most mammalian cells. The cell peripheries show higher sodium signals due to adhering of the nutrient medium to the edges of the cells and are ignored for quantitative calculations. The ^{40}Ca image from the same cells (Fig. 2*d*) reveals distinctly lower total calcium concentrations in the nuclei as compared with the cytoplasm, which is plausibly due to the presence of calcium-sequestering organelles in the cell cytoplasm (12). The ^{11}B and ^{19}F subcellular distributions from these cells are shown in Fig. 2, *e* and *f*, respectively. The ^{11}B is heterogeneously distributed throughout the cell with a distinctly lower concentration in the perinuclear organelle-rich cytoplasmic region (*arrows* in Fig. 2, *a* and *e*). The ^{19}F distribution in the same cell reveals similar patterns of subcellular gradients with the lowest levels in the same organelle-rich perinuclear region as identified in the boron image (*arrows* in Fig. 2, *a*, *e*, and *f*).

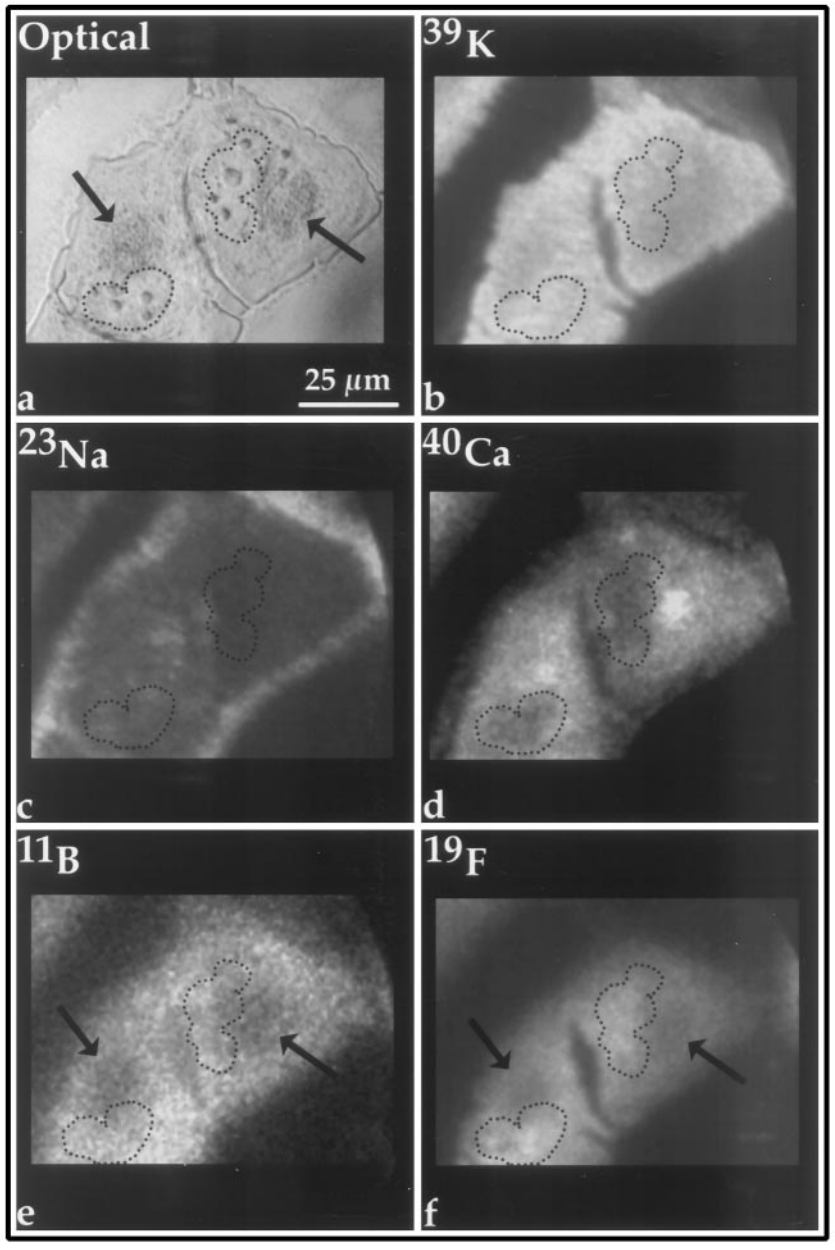

Fig. 2 SIMS isotope images of T98G human glioblastoma cells treated with 110 μg/ml boron equivalent of ^{19}F-BPA for 6 h. In the reflected light image (*a*), two fractured freeze-dried cells are shown with discernible nuclei (*dotted lines*) and a perinuclear organelle-rich cytoplasmic region (*arrows*). SIMS analysis of the same cells revealing subcellular isotopic distributions of ^{39}K (*b*), ^{23}Na (*c*), ^{40}Ca (*d*), ^{11}B (*e*), and ^{19}F (*f*) is shown. The *areas within the dotted lines* show the position of the nuclei, and *arrows* indicate the organelle-rich perinuclear cytoplasmic region in SIMS images.

It should be noted that the overall appearance of the boron and fluorine SIMS images (Fig. 2, *e* and *f*) is not identical, even though they reveal similar patterns of subcellular gradients. This is due to the fact that ionization potentials and SIMS sensitivities for detection are very different for these two elements. Under these experimental conditions, SIMS is much more sensitive to the detection of fluorine than boron. This is reflected by the fact that the boron image required 2 min of sputtering for image integration in comparison with 10 s for fluorine. A possible cocompartmentalization of fluorine and boron in subcellular compartments is indicated by these images (see more details in the results below). A nearly homogeneous ^{12}C image was also recorded from these cells (data not shown) to obtain the intracellular boron, potassium, and sodium concentrations (discussed later in the "Results" section).

Correlative Optical, CLSM, and SIMS Imaging of Fluorine and Boron in the Same Cell from ^{19}F-BPA-treated Cells. To confirm that a high density of mitochondria is present in the organelle-rich perinuclear cytoplasmic region that shows lower boron and fluorine signals, a correlative CLSM and SIMS ion microscopy approach was used. For these studies, in the last 30 min of the 6-h ^{19}F-BPA treatment, the cells were also labeled with a fluorescent mitochondria-specific stain, rhodamine 123, before cryogenic sampling. An example of the correlative optical, CLSM, and SIMS analysis of T98G cells treated with ^{19}F-BPA is shown in Fig. 3. The *top two panels* in the

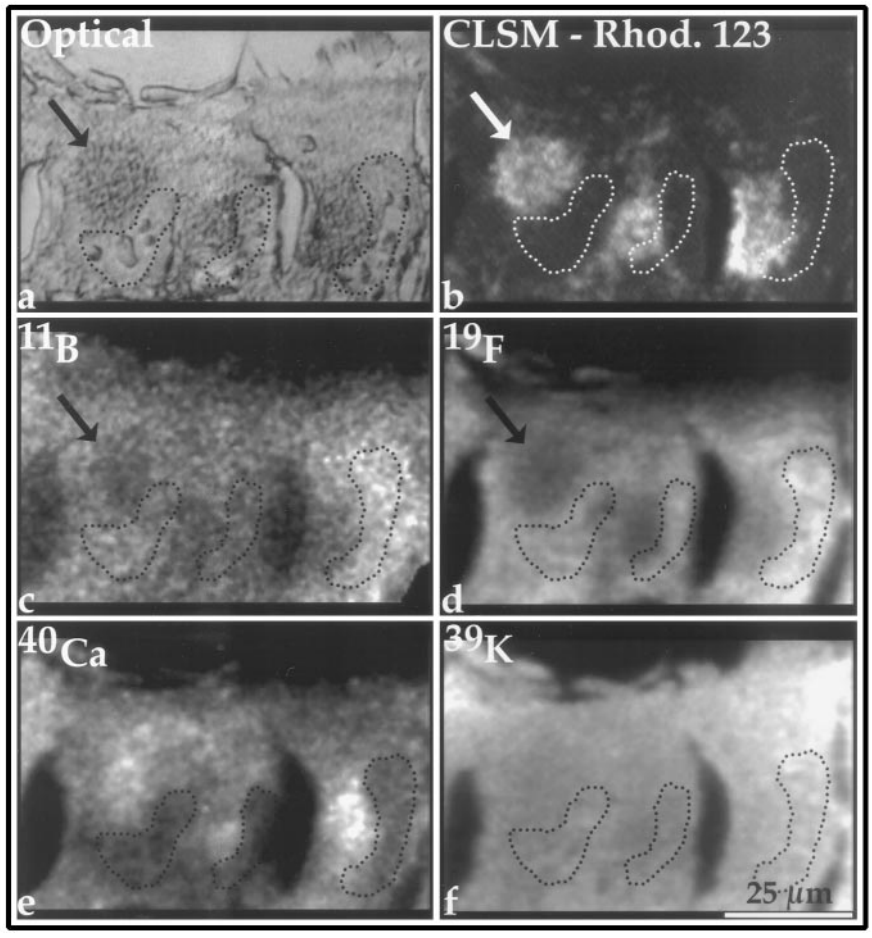

Fig. 3 Correlative optical, CLSM, and SIMS imaging of T98G human glioblastoma cells treated with 110 μg/ml boron equivalent of ^{19}F-BPA for 6 h. For the last 30 min of this treatment, the cells were also exposed to rhodamine 123 for labeling mitochondria. In the reflected light image (*a*), three fractured freeze-dried cells are shown with discernible nuclei (*dotted lines*) and the perinuclear organelle-rich cytoplasmic regions (the *arrow* points to one such region). CLSM imaging of rhodamine 123 fluorescence in the same cells (*b*) reveals high density of mitochondria in the perinuclear organelle-rich regions (the *arrow* points to one such region). SIMS analysis of the same cells revealing subcellular isotopic distributions of ^{11}B (*c*), ^{19}F (*d*), ^{40}Ca (*e*), and ^{39}K (*f*) is shown. The *areas within the dotted lines* show the position of the nuclei, and the *arrow* points to one organelle-rich perinuclear cytoplasmic region in SIMS images of boron and fluorine.

composite image show the optical (Fig. 3*a*) and the CLSM image of the rhodamine 123 fluorescence (Fig. 3*b*), revealing morphology in relation to mitochondrial distribution in individual fractured freeze-dried T98G cells. The boundaries of nuclei have been outlined with a *dotted line*, and an *arrow* indicates the organelle-rich perinuclear region in one cell (Fig. 3, *a* and *b*). The organelle-rich perinuclear regions correlate very well with the high mitochondrial density regions observed in each cell. These observations are consistent with a transmission electron microscopy study of T98G cells in which clusters of mitochondria were observed in perinuclear regions (28). SIMS analysis of these cells for ^{11}B, ^{19}F, ^{40}Ca, and ^{39}K is shown in Fig. 3, *c–f*, respectively. A comparable distribution of boron (Fig. 3*c*) and fluorine (Fig. 3*d*) was observed because both species showed significantly lower accumulation in the mitochondria-rich perinuclear region in each cell as compared with the remaining cytoplasm or the nuclei. The ^{40}Ca (Fig. 3*e*) and ^{39}K (Fig. 3*f*) images from the same cell show typical distributions as shown and discussed above in Fig. 2. Images of ^{12}C and ^{23}Na were also recorded from the same cells (data not shown).

Correlative Optical, CLSM, and SIMS Imaging of Boron from Nonfluorinated BPA. To observe whether the ^{19}F-BPA delivered boron to the same intracellular sites as the nonfluorinated BPA, T98G cells were treated with 110 μg/ml boron equivalent concentration of BPA for 6 h. For the last 30 min of this treatment, the cells were also exposed to rhodamine 123 for correlative CLSM and SIMS imaging. Fig. 4 shows an example of a correlative optical, CLSM, and SIMS analysis of fractured freeze-dried T98G glioblastoma cells from this treatment. The optical image (Fig. 4*a*) shows discernible nuclei and a perinuclear organelle-rich cytoplasmic region in each cell. The boundaries of nuclei have been outlined with a *dotted line* for the ease of matching them between the different images. The CLSM image of rhodamine 123 fluorescence from the same cells (Fig. 4*b*) reveals a region of higher mitochondrial density that correlates very well with the perinuclear organelle-rich cytoplasmic regions observed in the optical image in each cell (Fig. 4*a*). SIMS imaging of the same cells for ^{40}Ca and ^{10}B isotopic distributions is shown in Fig. 4, *c* and *d*, respectively. The total calcium distribution, as observed before, indicates the nuclei to be distinctly lower in calcium than the cytoplasm (Fig. 4*c*). The subcellular distribution of ^{10}B reveals a lower accumulation in the mitochondria-rich perinuclear region in each cell as compared with the remaining cytoplasm or the nuclei. This subcellular distribution of ^{10}B from ^{10}BPA is virtually indistinguishable from the subcellular distribution of ^{11}B from ^{19}F-^{11}BPA. Images of ^{39}K, ^{23}Na, and ^{12}C were also recorded from these cells (data not shown).

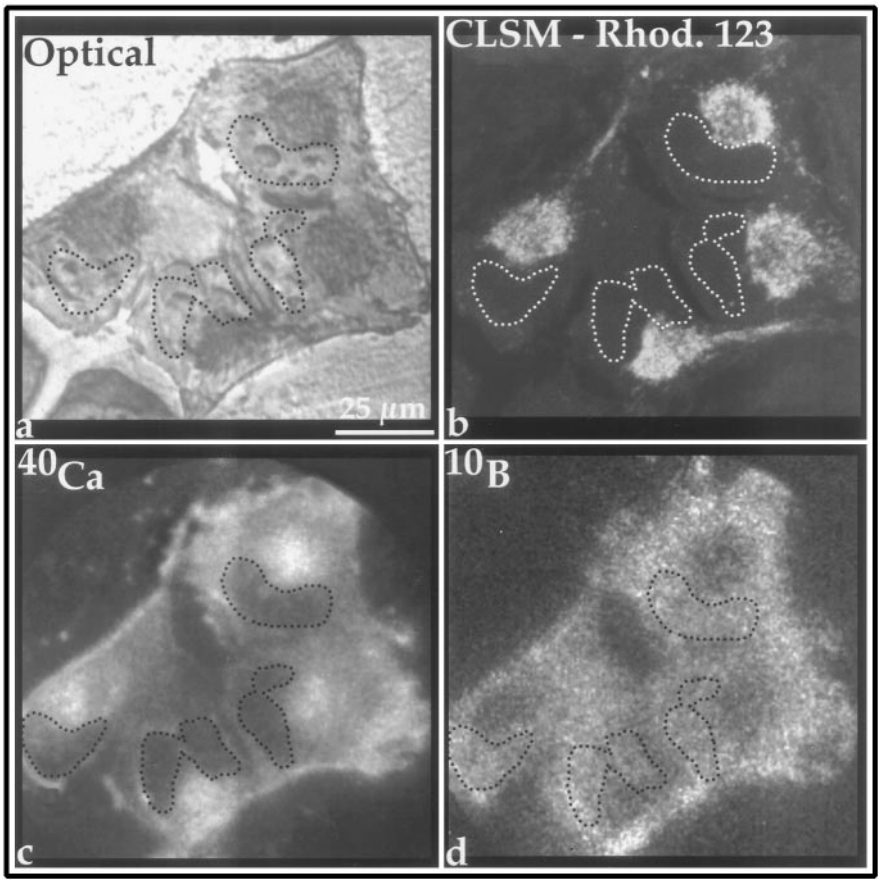

Fig. 4 Correlative optical, CLSM, and SIMS imaging of T98G human glioblastoma cells treated with 110 μg/ml boron equivalent of BPA for 6 h. For the last 30 min of this treatment, the cells were also exposed to rhodamine 123 for labeling mitochondria. In the reflected light image (*a*), four fractured freeze-dried cells are shown with discernible nuclei (*dotted lines*) and the perinuclear organelle-rich cytoplasmic regions. CLSM imaging of rhodamine 123 fluorescence in the same cells (*b*) reveals high density of mitochondria in the perinuclear organelle-rich regions. SIMS analysis of the same cells revealing subcellular isotopic distributions of ^{40}Ca (*c*) and ^{10}B (*d*) is shown. The *areas within the dotted lines* show the position of the nuclei.

Table 1 Intracellular concentrations of potassium, sodium, and boron in T98G human glioblastoma cells after treatment with either ^{19}F-BPA or BPA

Cellular potassium and sodium concentrations (mean ± SE) and subcellular boron concentrations (mean ± SE) in T98G human glioblastoma cells treated with 110 μg/ml boron equivalent of ^{19}F-BPA or BPA for 6 h are shown. Concentrations of potassium and sodium are expressed in mM on a cellular scale. Concentrations of boron are expressed in μg/g wet weight in the nucleus, mitochondria-rich perinuclear cytoplasm, and the remaining cytoplasm of T98G cells. The number of cells used for quantitative calculations and the number of SIMS imaging fields are also listed.

Boronated compound	Cellular potassium (mM)	Cellular sodium (mM)	μg/g Boron (wet weight)			No. of cells	No. of SIMS imaging fields
			Nucleus	Mitochondria-rich perinuclear cytoplasm	Remaining cytoplasm		
^{19}F-BPA	165 ± 6	18 ± 1	289 ± 10	225 ± 9	302 ± 11	35	7
BPA	165 ± 8	17 ± 1	281 ± 8	189 ± 6	280 ± 10	33	6

Quantitative Comparison of Intracellular Potassium, Sodium, and Subcellular Boron Concentrations in T98G Glioblastoma Cells from ^{19}F-BPA and BPA Treatments. Table 1 shows a quantitative comparison of intracellular potassium, sodium, and boron concentrations in T98G glioblastoma cells after ^{19}F-BPA and BPA treatments. The concentrations of potassium and sodium are expressed on a cellular level. Boron concentrations were calculated in subcellular compartments of the nucleus, the mitochondria-rich perinuclear cytoplasm, and the remaining cytoplasm. The T98G cells from both treatments contained approximately 165 mM potassium and 17 mM sodium. These concentrations indicate that even the most highly diffusible intracellular species were well preserved by the cryogenic sample preparation used in the study. The subcellular boron concentrations from both ^{19}F-BPA and BPA were not significantly different (Table 1). The perinuclear mitochondrial-rich cytoplasmic region accumulated significantly less ($P \leq 0.01$) boron from either compound as compared with the remaining cytoplasm or the nuclei. Furthermore, the addition of rhodamine 123 caused no significant difference in the concentrations of any species discussed here.

A Comparison of Subcellular Fluorine and Boron Signals from F-BPA-treated Cells. A comparison of fluorine and boron distributions in subcellular compartments was made

by calculating the ^{19}F:^{12}C and ^{11}B:^{12}C ratios of signal intensities in the nucleus, the mitochondria-rich perinuclear cytoplasm, and the remaining cytoplasm of individual cells. The ^{19}F:^{12}C or ^{11}B:^{12}C ratio in the perinuclear region (or in the remaining cytoplasm) was then normalized to the respective ratio from the nuclei. In comparison with the cell nuclei, the mitochondria-rich perinuclear region contained 71 ± 8% boron and 75 ± 11% fluorine, whereas the remaining cytoplasm contained 105 ± 10% boron and 96 ± 14% fluorine (mean ± SD, $n = 25$ cells from five SIMS imaging fields). These observations support a probable intracellular cocompartmentalization of fluorine and boron in F-BPA-treated cells.

DISCUSSION

Fluorinated compounds are becoming increasingly valuable in medicine due to their therapeutic and diagnostic characteristics. Fluorinated nucleosides have been shown to possess antitumor and antiproliferative characteristics (29, 30). The tagging of radioactive fluorine (^{18}F) in desired compounds enables the diagnostic imaging of tumors by noninvasive techniques such as PET. Similarly, compounds labeled with the stable isotope of fluorine (^{19}F) can be used for MRI. Indeed, fluorinated analogues of compounds such as 2-fluoro-2-deoxy-D-glucose and dihydroxyphenylalanine have become popular imaging agents for diagnostic PET and MRI studies of humans (31–34). In general, the spatial resolution for MRI and PET techniques may range from low millimeters to a centimeter (31, 35–37), and this restriction limits the analysis to gross tissues (*e.g.*, tumors) rather than clusters of a few cells, single cells, and subcellular compartments. The single-cell subcellular information is generally desired for understanding the mode of action, intracellular targeting, and metabolic characteristics of many therapeutic/diagnostic agents. Microanalytical techniques that provide this information cannot be used directly on humans but rely on sampling of the tumor tissue or the use of cell culture model systems. Alpha track autoradiography, commonly used for radiation dosimetry studies in BNCT, is specific for the detection of ^{10}B alone (38) and hence cannot be used for the present study. SIMS ion microscopy, however, is ideally suited for the present study because it is capable of subcellular imaging of a number of desired elements (isotopes) in the same cell with high sensitivity.

The present study required further methodological development for SIMS analysis of organelle level fluorine and boron distributions from F-BPA in the same cell. This was achieved by using correlative CLSM and SIMS on the same cryogenically prepared cell. Our observations of fluorine and boron on subcellular distributions from F-BPA suggest that intracellular boron and fluorine are cocompartmentalized. This conclusion is also supported by the observation of a comparable delivery of boron to subcellular compartments by fluorinated and nonfluorinated BPA as well as the partitioning of boron and fluorine in cellular compartments. In the present study, the imaging of fluorine and boron along with potassium and sodium from the same cell provides confidence in measurements and an internal check of the reliability of sample preparation. Indeed, the potassium and sodium concentrations observed in T98G cells (Table 1) reflect physiologically relevant concentrations of these ions in most mammalian cells. The mitochondria-rich perinuclear region does not show any noticeable gradient of potassium and sodium, as observed for fluorine and boron distributions, and rules out the possibility of any special characteristics (*e.g.*, SIMS matrix effects; the degree of hydration) of this region that will significantly affect SIMS images. Because mitochondria are the principal contributors to the SIMS sampling of this perinuclear cytoplasmic region, the present study indicates the possibility of a reduced uptake of these compounds in mitochondria. Alternatively, other organelles and sequestering mechanisms may also be at work in this organelle-rich perinuclear cytoplasmic region, which may affect the local concentration of these compounds.

The subcellular boron concentrations from both F-BPA and nonfluorinated BPA indicate that the boron partitioning between the cells and the extracellular medium has more than doubled within 6 h of treatment (see Table 1 in relation to 110 μg/ml extracellular boron in the medium). It is remarkable that this pattern of boron uptake was also observed in infiltrating tumor cells in the normal brain of the 9L rat gliosarcoma model (39). Furthermore, recent observations on ^{19}F-BPA with nuclear magnetic resonance on a relatively large population of cells (over 50 million or so) revealed the near doubling of the ^{19}F nuclear magnetic resonance signal within 3 h of drug exposure (40). The rationale for use of the 6-h treatment was provided by other ion microscopy studies exploring the time-dependent accumulation of boron uptake from BPA in T98G cells (41) and in the rat 9L gliosarcoma brain tumor model, where tumor cells infiltrating the normal brain gained significantly higher levels of boron from a continuous 6-h i.v. infusion protocol as compared with 2- and 3-h infusions (39). Indeed, the observations made in these cell culture and animal model studies have provided the foundation for new clinical trials of BNCT in Sweden, where the 6-h infusion protocol for BPA administration is currently being evaluated for the treatment of glioblastoma multiforme. The mechanism of higher boron uptake from BPA at 6 h, and possibly beyond, is not known but may involve an increase in the bound form of either BPA or its boronated metabolite inside the cell. In a recent study on cell cultures, it was reported that BPA is actively transported through the cell membrane by the L amino acid transport system and that malignant cells can use larger amounts due to their increased metabolism (42).

The implications of the present work are clear for the PET imaging studies for BNCT that were made using the assumption that the biological properties of the ^{18}F-labeled compound are the same as the clinical agent, BPA (8, 9). Fortunately, nonradioactive ^{19}F-labeled BPA can be used in SIMS ion microscopy studies, where the critical information of subcellular fluorine localization (as well as boron delivery) can be determined for pharmacological concentrations. This is critical information in the development of PET as a viable tool for BNCT because kinetic parameters of the tracer uptake, determined using very low concentrations of the radionuclide ^{18}F-labeled compound, must be extrapolated to clinically relevant concentrations.

The present study suggests that the fluorine and boron from ^{19}F-BPA are cocompartmentalized at the subcellular scale and that ^{19}F-BPA delivers boron to intracellular compartments in concentrations comparable with the nonfluorinated clinically approved drug BPA. These valuable observations provide strong

support for the use of F-BPA in PET scan studies of brain tumors for pharmacokinetic evaluations of ^{18}F-BPA. Because the radionuclide ^{18}F is a widely used tracer used in very low concentrations for PET imaging in medicine, a correlative SIMS and CLSM approach for the quantitative imaging of fluorine at subcellular resolution could have implications far beyond BNCT, such as by playing a major role in the development and validation of new radiotracers for PET applications.

REFERENCES

1. Sweet, W. H. The uses of nuclear disintegration in the diagnosis and treatment of brain tumor. N. Engl. J. Med., *245:* 875–878, 1951.

2. Barth, R. F, Soloway, A. H., and Fairchild, R. G. Boron neutron capture therapy for cancer. Sci. Am. *263:* 100–103, 106–107, 1990.

3. Slatkin, D. N. A history of boron neutron capture therapy of brain tumors. Brain, *114:* 1609–1629, 1991.

4. Coderre, J. A., and Morris, G. M. The radiation biology of boron neutron capture therapy. Radiat. Res., *151:* 1–18, 1999.

5. Mishima, Y., Ichihashi, M., Honda, C., Shiono, M., Nakagawa, T., Obara, H., Shirakawa, J., Hiratsuka, J., Kanda, K., Kobayashi, T., Nozaki, T., Aizawa, O., Sato, T., Karashima, H., Yoshino, K., and Fukuda, H. Advances in the control of cutaneous primary and metastatic melanoma by thermal neutron capture therapy. *In:* B. J. Allen, D. E. Morre, and B. V. Harrington (eds.), Progress in Neutron Capture Therapy for Cancer, pp. 577–583. New York: Plenum Press, 1992.

6. Gabel, D., Foster, S., and Fairchild, R. G. The Monte Carlo simulation of the biological effect of the ^{10}B(n,α)^{7}Li reaction in cells and tissue and its implications for boron neutron capture therapy. Radiat. Res., *111:* 14–25, 1987.

7. Charlton, D. E. Energy deposition in small ellipsoidal volumes by high-LET particles: application to thermal neutron dosimetry. Int. J. Radiat. Biol., *59:* 827–842, 1991.

8. Kabalka, G. W., Smith, G. T., Dyke, J. P., Reid, W. S., Longford, C. P. D., Roberts, T. G., Reddy, N. K., Buonocore E., and Hübner, K. F. Evaluation of fluorine-18-BPA-fructose for boron neutron capture treatment planning. J. Nucl. Med., *38:* 1762–1767, 1997.

9. Imahori, Y., Ueda, S., Ohmori, Y., Kusuki, T., Ono, K., Fujii, R., and Ido, T. Fluorine-18-labeled fluoroboronophenylalanine PET in patients with glioma. J. Nucl. Med., *39:* 325–333, 1998.

10. Chandra, S., Smith, D. R., and Morrison, G. H. Subcellular imaging by dynamic SIMS ion microscopy. Anal. Chem., *72:* 104A−114A, 2000.

11. Smith, D. R., Chandra, S., Coderre, J. A., and Morrison, G. H. Ion microscopy imaging of ^{10}B from *p*-boronophenylalanine in a brain tumor model for boron neutron capture therapy. Cancer Res., *56:* 4302–4306, 1996.

12. Chandra, S., Kable, E. P. W., Morrison, G. H., and Webb, W. W. Calcium sequestration in the Golgi apparatus of cultured mammalian cells revealed by laser scanning confocal microscopy and ion microscopy. J. Cell Sci., *100:* 747–752, 1991.

13. Kabalka, G. W., Reddy, N. K., Wang, L., and Malladi, R. R. Synthesis of 4-borono-2-fluorophenylalanine. Org. Prep. Proced. Int., *32:* 290–293, 2000.

14. Coderre, J. A., Button, T. M., Micca, P. L., Fischer, C., Nawrocky, M. M., and Liu, H. B. Neutron capture therapy of the 9L rat gliosarcoma using the *p*-boronophenylalanine-fructose complex. Int. J. Radiat. Oncol. Biol. Phys., *30:* 643–652, 1994.

15. Chandra, S., and Morrison, G. H. Imaging elemental distribution and ion transport in cultured cells with ion microscopy. Science (Wash. DC), *228:* 1543–1544, 1985.

16. Chandra, S., and Morrison, G. H. Ion microscopy in biology and medicine. Methods Enzymol., *158:* 157–179, 1988.

17. Zha, X., Ausserer, W. A., and Morrison, G. H. Quantitative imaging of a radiotherapeutic drug $Na_2B_{12}H_{11}SH$ at subcellular resolution in tissue cultures using ion microscopy. Cancer Res., *52:* 5219–5222, 1992.

18. Chandra, S., and Lorey, D. R., II. SIMS ion microscopy in cancer research: single cell isotopic imaging for chemical composition, cytotoxicity, and cell cycle regulation. Cell. Mol. Biol., *47:* 503–518, 2001.

19. Lorey, D. R., II, Morrison, G. H, and Chandra, S. Dynamic SIMS analysis of boron from BNCT drugs in co-cultures: single cell imaging of two different cell types within the same ion microscopy field of imaging. Anal. Chem., *73:* 3947–3953, 2001.

20. Chandra, S., Morrison, G. H., and Wolcott, C. C. Imaging intracellular elemental distribution and ion fluxes in cultured cells with ion microscopy: A freeze-fracture methodology. J. Microsc. (Oxf.), *144:* 15–37, 1986.

21. Fairchild, R. G., Gabel, D., Laster, B. H., Greenberg, D., Kiszenick, W., and Micca, P. L. Microanalytical techniques for boron analysis using the ^{10}B(n,α)^{7}Li reaction. Med. Phys., *13:* 50–56, 1986.

22. Johnson, L. V., Walsh, M. L., and Chen, L. B. Localization of mitochondria in living cells with rhodamine 123. Proc. Natl. Acad. Sci. USA, *77:* 990–994, 1980.

23. Chandra, S., and Morrison, G. H. Evaluation of fracture planes and cell morphology in complimentary fractures of cultured cells in the frozen-hydrated state by field-emission secondary electron microscopy: feasibility for ion localization and fluorescence imaging studies. J. Microsc. (Oxf.), *186:* 232–245, 1997.

24. Chandra, S., and Morrison, G. H. Sample preparation of animal tissues and cell cultures for secondary ion mass spectrometry (SIMS) microscopy. Biol. Cell, *74:* 31–42, 1992.

25. Chandra, S., Ausserer, W. A., and Morrison, G. H. Evaluation of matrix effects in ion microscopic analysis of freeze-fractured, freeze-dried cultured cells. J. Microsc. (Oxf.), *148:* 223–239, 1987.

26. Ausserer, W. A., Chandra, S., and Morrison, G. H. Morphological and elemental integrity of freeze-fractured, freeze-dried cultured cells during ion microscopic analysis. J. Microsc. (Oxf.), *154:* 39–57, 1988.

27. Ausserer, W. A., Ling, Y-C., Chandra, S., and Morrison, G. H. Quantitative imaging of boron, calcium, magnesium, potassium, and sodium in cultured cells. Anal. Chem., *61:* 2690–2695, 1989.

28. Weller, M., Winter, S., Schmidt, C., Esser, P., Fontana, A., Dichgans, J., and Groscurth, P. Topoisomerase-I inhibitors for human malignant glioma: differential modulation of p53, p21, bax and bcl-2 expression and of CD95-mediated apoptosis by camptothectin and b-lapachone. Int. J. Cancer, *73:* 707–714, 1997.

29. Brix, G., Bellemann, M. E., Haberkorn, U., Gerlach, L., and Lorenz, W. J. Assessment of the biodistribution and metabolism of 5-fluorouracil as monitored by ^{18}F PET and ^{19}F MRI: a comparative animal study. Nucl. Med. Biol., *23:* 897–906, 1996.

30. Tanaka, Y., Eda, H., Fujimoto, K., Tanaka, T., Ishikawa, T., and Ishitsuka, H. Anticachectic activity of 5′-deoxy-5-fluorouridine in a murine tumor cachexia model colon 26 adenocarcinoma. Cancer Res., *50:* 4528–4532, 1990.

31. Ross, B., and Bluml, S. Magnetic resonance spectroscopy of the human brain. Anat. Rec. (New Anat.), *265:* 54–84, 2001.

32. Van der Hiel, B., Pauwels, E. K. J., and Stokkel, M. P. M. Positron emission tomography with 2-[^{18}F]-fluoro-2-deoxy-D-glucose in oncology. J. Cancer Res. Clin. Oncol., *127:* 269–277, 2001.

33. Rousset, O. G., Deep, P., Kuwabara, H., Evans, A. C., Gjedde, A. H., and Cumming, P. Effect of partial volume correction on estimates of the influx and cerebral metabolism of 6-[^{18}F]fluoro-L-DOPA studied with PET in normal control and Parkinson's disease subjects. Synapse, *37:* 81–89, 2000.

34. Kahn, D., Follett, K. A., Bushnell, D. L., Nathan, M. A., Piper, J. G., Madsen, M., and Kirchner, P. T. Diagnosis of recurrent brain tumor: value of ^{201}Tl SPECT *versus* ^{18}F-fluorodeoxyglucose PET. Am. J. Roentgen., *163:* 1459–1465, 1994.

35. Kunze, W. D., Baehre, M., and Richter, E. PET with a dual-head coincidence camera: spatial resolution, scatter fraction, and sensitivity. J. Nucl. Med., *41:* 1067–1074, 2000.

36. Lundqvist, H., Lubberink, M., Tolmachev, V., Lovqvist, A., Sundin, A., Beshara, S., Bruskin, A., Carlsson, J., and Westlin, J. E.

Positron emission tomography and radioimmunotargeting: general aspects. Acta Oncol. (Stockholm), *38:* 335–341, 1999.

37. Gunnar, B., Bellemann, M. E., Haberkorn, U., Gerlach, L., Bachert, P., and Lorenz, W. J. Mapping the biodistribution and catabolism of 5-fluorouracil in tumor-bearing rats by chemical-shift selective ^{19}F MR imaging. Magn. Reson. Med., *34:* 302–307, 1995.

38. Solares, G. R., and Zamenhof, R. G. A novel approach to the microdosimetry of neutron capture therapy. Part 1. High-resolution quantitative autoradiography applied to microdosimetry in neutron capture therapy. Radiat. Res., *144:* 50–58, 1995.

39. Smith, D. R., Chandra, S., Barth, R. F., Yang, W., Joel, D. D., and Coderre, J. A. Quantitative imaging and microlocalization of boron-10 in brain tumors and infiltrating tumor cells by SIMS ion microscopy: relevance to neutron capture therapy. Cancer Res., *61:* 8179–8187, 2001.

40. Panov, V., Salomon, Y., Kabalka, G. W., and Bendel, P. Uptake and washout of borocaptate sodium and borono-phenylalanine in cultured melanoma cells: a multi-nuclear NMR study. Radiat. Res., *154:* 104–112, 2000.

41. Chandra, S., Lorey, D. R., II, and Smith, D. R. Quantitative subcellular dynamic SIMS imaging of boron-10 and boron-11 isotopes in the same cell delivered by two combined BNCT drugs: *in vitro* studies on human glioblastoma T98G cells. Radiat. Res., *157:* 700–710, 2002.

42. Wittig, A., Sauerwein, W. A., and Coderre, J. A. Mechanisms of transport of *p*-borono-phenylalanine through the cell membrane *in vitro*. Radiat. Res., *153:* 173–180, 2000.

Clinical Cancer Research

Imaging of Fluorine and Boron from Fluorinated Boronophenylalanine in the Same Cell at Organelle Resolution by Correlative Ion Microscopy and Confocal Laser Scanning Microscopy

Subhash Chandra, George W. Kabalka, Daniel R. Lorey II, et al.

Clin Cancer Res 2002;8:2675-2683.